

Relativistic MHD with central-type schemes

Axisymmetric simulations of Pulsar Wind Nebulae

L. Del Zanna

Dipartimento di Astronomia e Scienza dello Spazio, Università di Firenze

Abstract. A third order shock-capturing numerical scheme for three-dimensional special relativistic magnetohydrodynamics (3-D RMHD) is presented and validated against several numerical tests of astrophysical interest. Due to the difficulties in developing exact or even approximate Riemann solvers in RMHD, a simple two-speed central-type solver that requires the knowledge of only the local fast magnetosonic velocities is employed. We show here that the combination of high order reconstruction with a simplified solver provides an efficient, accurate and robust scheme. First results from axisymmetric simulations of Pulsar Wind Nebulae (PWNe) are finally presented.

Key words. magnetohydrodynamics (MHD) – relativity – shock waves – methods: numerical

1. Introduction

Relativistic fluid dynamics and magnetohydrodynamics (MHD) play a fundamental role in the investigation of the astrophysical sources of high-energy radiation and particles. Examples are provided by Active Galactic Nuclei (AGNs) and associated radio jets, galactic compact X-ray sources (e.g. microquasars), Gamma-Ray Bursts (GRBs), and pleionic supernova remnants (or Pulsar Wind Nebulae, PWNe). It should be clear that only computer simulations can follow the evolution of such complex phenomena, thus there is a great interest in developing numerical codes for relativistic flows.

In the last decade the conservative Godunov-type numerical schemes, which

had been already successfully applied to gasdynamic problems, have started to be widely applied to relativistic hydrodynamics (RHD: e.g. Donat et al. 1998; Aloy et al. 1999; Del Zanna & Bucciantini 2002; see Marti & Müller 2003 for a review), to relativistic magnetohydrodynamics (RMHD: Komissarov, 1999; Del Zanna et al., 2003, DZ hereafter), and even to general relativistic MHD with a fixed metric (GRMHD: Koide et al. 1996, 1999; Gammie et al. 2003; see Font 2003 for a review, including methods for coupling the fluid schemes to solvers for the Einstein equations).

While most of the hydro codes rely on complex characteristics based Riemann solvers, in RMHD and GRMHD the choice is usually to apply simplified solvers that do not require spectral decomposition, because of non strict hyperpolicity of the system (eigenvalue

Correspondence to: Largo E. Fermi 2, 50125 Firenze, ldz@arcetri.astro.it

degeneracies). These schemes are often referred to as *central schemes*: reconstruction is applied component-wise and the Riemann fan at inter-cells is averaged to provide a single intermediate state (e.g. Lax-Friedrichs solver). Another difficulty in *multidimensional* MHD systems is how to formulate reconstruction procedures and (approximate) Riemann solvers sharing consistency with the divergence-free constraint (e.g. Toth 2000; Londrillo & Del Zanna 2000, 2004).

In this paper we summarize the main features of the central-type *third-order* RMHD scheme of DZ, based on a two-speed HLL central-upwind approximate solver and ENO-type reconstruction routines. We show here that the combination of high order reconstruction with a simplified solver provides an efficient, accurate and robust scheme. First results from axisymmetric simulations of Pulsar Wind Nebulae are finally presented.

2. The RMHD equations and the numerical scheme

As their classical MHD counterpart, the fluid RMHD equations retain the usual conservative form, needed for any shock-capturing scheme:

$$\frac{\partial \mathbf{u}}{\partial t} + \sum_{i=1}^3 \frac{\partial \mathbf{f}^i}{\partial x^i} = 0.$$

Here \mathbf{u} is the vector of conserved variables and \mathbf{f}^i are their corresponding fluxes, along each direction, respectively given by

$$\mathbf{u} = [\rho u^0, w_i u^0 u^j - b^0 b^j, w_i u^0 u^0 - b^0 b^0 - p_i]^T,$$

$$\mathbf{f}^i = [\rho u^i, w_i u^i u^j - b^i b^j + p_i \delta^{ij}, w_i u^0 u^i - b^0 b^i]^T,$$

where we have defined $w_i = w + |b|^2$ and $p_i = p + |b|^2/2$. Here $u^\alpha = (\gamma, \gamma v^j)$ is the four-velocity, $\gamma \equiv u^0 = (1 - v^2)^{-1/2}$ is the Lorentz factor, $w = e + p$ is the relativistic enthalpy ($e = \rho + p/(\Gamma - 1)$ is the relativistic energy per unit volume for a Γ -law equation of state). The components of the magnetic four-vector are

$$b^\alpha = [\gamma(\mathbf{v} \cdot \mathbf{B}), \mathbf{B}/\gamma + \gamma(\mathbf{v} \cdot \mathbf{B})\mathbf{v}],$$

and in the fluid comoving local rest frame we simply have $b^\alpha = (0, \mathbf{B})$. Note the constraints

$$u_\alpha b^\alpha = 0 \text{ and } |u|^2 \equiv u_\alpha u^\alpha = -1, \text{ so that } |b|^2 \equiv b_\alpha b^\alpha > 0 \text{ and } b^\alpha \text{ is a space-like vector, with } |b|^2 = B^2/\gamma^2 + (\mathbf{v} \cdot \mathbf{B})^2.$$

On the other hand, the covariant equation for b^α splits into two parts, which happen to be exactly the same as in classical MHD (this is not surprising since Maxwell equations are Lorentz invariant). The spatial component gives the classical induction equation

$$\frac{\partial \mathbf{B}}{\partial t} + \nabla \times \mathbf{E} = 0; \quad \mathbf{E} = -\mathbf{v} \times \mathbf{B},$$

which is properly the time evolution equation for \mathbf{B} . Note that the spatial differential operator is in a *curl* form, rather than in a *divergence* form as the energy-momentum conservation law. This means that the evolution equation of each spatial component of \mathbf{B} has a missing eigen-space, basically due to the antisymmetry of the electromagnetic tensor. Thus, a total of just three independent magnetic fluxes (the electric field vector components, just one in 2-D) are needed for the evolution of \mathbf{B} , while six independent fluxes were required for the momentum evolution. The other consequence of the tensor antisymmetric nature is that the time component of the covariant equation for b^α becomes the usual MHD solenoidal constraint

$$\nabla \cdot \mathbf{B} = 0,$$

which is *not* an evolutionary equation but a differential constraint on the spatial derivatives of \mathbf{B} . This constraint is usually regarded as just an initial condition, since the form of the induction equation assures its preservation in time. Unfortunately this property does not hold in upwind numerical schemes, which instead must be designed in a way that the specific divergence-free nature of the magnetic field is taken into account as a fundamental constitutive property, otherwise spurious magnetic monopoles will affect the overall solution and often the code stability itself. The *Constrained Transport* staggered method (CT: Evans & Hawley 1988), originally designed for the induction equation alone, has been extended for any upwind scheme solving the overall set of MHD equations (*Upwind Constrained Transport*, UCT: see Londrillo &

Del Zanna 2004). Our RMHD code takes advantage of this method, thus the divergence-free constraint is preserved within machine accuracy at all times.

In the present section we briefly summarize the main points that characterize the RMHD scheme first described in DZ:

1. A third-order TVD Runge-Kutta cycle is used for time integration (Shu & Osher, 1988). The global time step is chosen to be proportional to the inverse of the largest *fast magneto-sonic* characteristic speed present in the computational domain.
2. Point values, rather than cell averages, are used to discretize fluid conservative variables at cell centers.
3. A robust and efficient iterative scheme is used to get primitive fluid variables (ρ, \mathbf{v}, p) from the set of conservative variables, by first projecting along the direction of the local magnetic field. The 5x5 set of equations is reduced down to just a couple of non-linear equation, where only one of them has to be solved numerically.
4. Third order Convex ENO routines (Liu & Osher, 1998; Londrillo & Del Zanna, 2000) with standard slope limiters (MinMod, Monotonized Centered) are employed for variables reconstruction at cell boundaries.
5. A two-speed solver (HLL: Harten et al. 1983) is used to define numerical fluxes at cell interfaces:

$$\mathbf{f} = \frac{\alpha^+ \mathbf{f}^L + \alpha^- \mathbf{f}^R - \alpha^+ \alpha^- (\mathbf{u}^R - \mathbf{u}^L)}{\alpha^+ + \alpha^-}.$$

Here the α^\pm coefficients take into account the highest speeds at the two sides of the Riemann fan, which can be estimated from the maximum and minimum eigenvalue λ^\pm of the Jacobians at the left and right reconstructed states:

$$\alpha^\pm = \max\{0, \pm \lambda^\pm(\mathbf{v}^L), \pm \lambda^\pm(\mathbf{v}^R)\}.$$

Notice that when the local Riemann fan is symmetric, then $\alpha^+ = \alpha^- = \alpha$ and the flux coincides with the simple local Lax-Friedrichs flux. Whereas, when both fast magneto-sonic speeds have the same sign one of the α^\pm is zero and the HLL flux becomes a pure upwind flux, either \mathbf{f}^L or \mathbf{f}^R .

6. In any CT-based MHD scheme the fundamental magnetic field components are discretized at cell interfaces. In our UCT scheme we also introduce a potential vector \mathbf{A} , from which the staggered field components are derived as $\mathbf{B} = \nabla \times \mathbf{A}$, which is defined and integrated in time at cell corners. The numerical flux for \mathbf{A} is the electric field \mathbf{E} , whose HLL upwind numerical expression is a four-state function (see DZ).

3. Code validation

3.1. 2-D numerical tests

Multidimensional tests (here just 2-D, see Del Zanna & Bucciantini 2002, for some 3-D RHD tests) truly prove the robustness of the code and, in particular, its accuracy in preserving $\nabla \cdot \mathbf{B} = 0$ in time, thus avoiding the onset of spurious forces due to the presence of numerical magnetic monopoles (we remind that the solenoidal constraint is preserved here within machine accuracy).

In the first test, a RMHD cylindrical blast wave, we use a $[0, 1] \times [0, 1]$ Cartesian grid with a resolution of $N_x = N_y = 250$ grid points, and we define an initially static background with $\rho = 1.0$, $p = 0.01$ and $B_x = 4.0$. A relativistic flow comes out by setting a much higher pressure, $p = 10^3$, within a circle of radius $r = 0.08$ placed at the center of the domain. Here we use $\Gamma = 4/3$. In Fig. 1 we show the situation at $t = 0.4$, when the flow has almost reached the outer boundaries. The flow speed reaches its maximum value along the x direction, $\gamma_{\max} \simeq 4.35$, because the expansion of the blast wave is not slowed down by the presence of a transverse magnetic field, as it happens along y where field lines are squeezed producing the highest magnetic pressure.

The same numerical parameters, but with a higher resolution ($N_x = N_y = 400$), are employed in the second simulation, here adapted to the relativistic case from the classical MHD one. A disk of radius 0.1 with higher density, $\rho = 10$, rotating at high relativistic speed, $\omega = 9.95 \Rightarrow \gamma_{\max} \simeq 10.0$, the *rotor*, is embedded in a static background with $\rho = 1.0$, $p = 1.0$ and

Blast 2-D: CENO3-HLL-MM, N=250, CFL=0.5

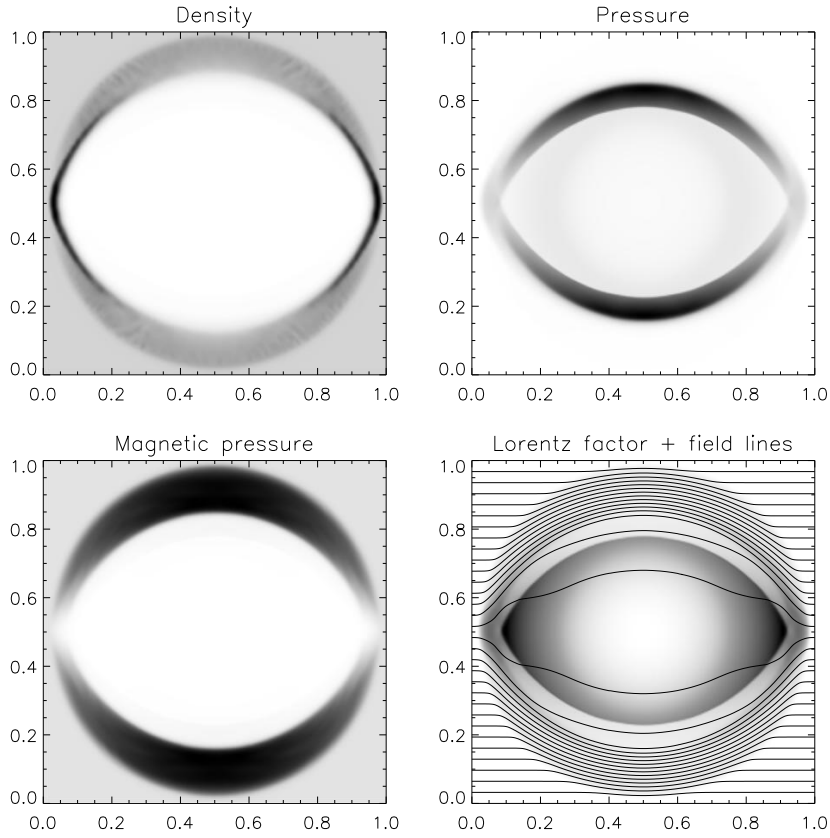


Fig. 1. A RMHD 2-D strong explosion with a pressure jump as high as 10^5 .

$B_x = 1.0$ ($\Gamma = 5/3$). In Fig. 2 the complicated pattern of shocks and torsional Alfvén waves launched by the rotor may be seen at the usual output time $t = 0.4$, when the central field lines are rotated of an angle of almost 90° .

Finally, as a typical astrophysical test, we simulate the propagation of an axisymmetric RHD jet in 2-D cylindrical coordinates (z, r) . Note that jet simulations are a very hard test for codes not based on characteristics decomposition, because of usually stronger numerical viscosity at shear layers. The domain is $0 < r < 8$ and $0 < z < 20$, with reflective boundary conditions on the axis $r = 0$ and simple extrapolation at the other boundaries (except at $z = 0$ within the jet radius, where initial

values are kept constant). At $t = 0$ a relativistic jet with $v_z = 0.99$ and density 100 times less than the surroundings (but same pressure) is located at $r \leq 1$ and $z \leq 1$. The jet evolution is followed until $t = 40$, as shown in Fig. 3, where density contours and gray shades in logarithmic scale are presented. The code settings are CENO3-HLL-MC, while the resolution employed is 400×160 , corresponding to 20 grid points per jet radius. Note that the smearing of contact discontinuities, unavoidable in methods not based on characteristics decomposition, is actually small and vortices due to Kelvin-Helmoltz instabilities are nicely defined, as well as the external bow shock, the internal Mach disk and other shocks reflected

Rotor: CENO3-HLL-MM, N=400, CFL=0.5

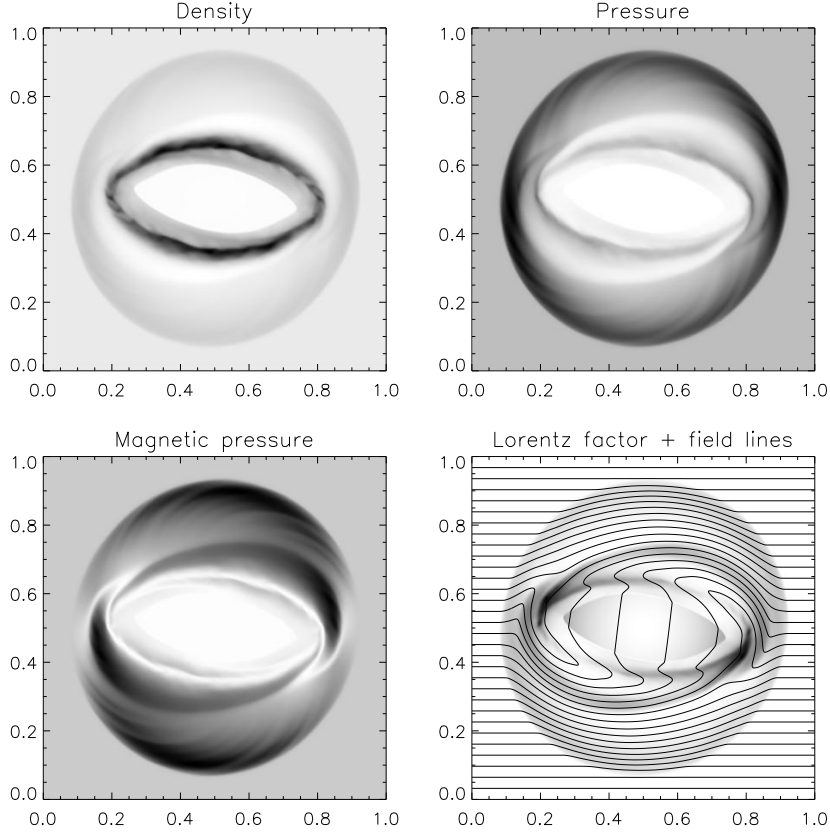


Fig. 2. The relativistic analog of the *rotor* test (initial maximum Lorentz factor of about 10).

off the axis. Moreover, notice the absence of the so-called *carbuncle* problem, usually manifesting as an extended *nose* in the front of the jet on the axis.

3.2. Convergence tests

In the present subsection we check the high resolution properties of the interpolation routines on smooth fields. In cases where discontinuous features are absent, these algorithms are designed to achieve third order accuracy.

To this purpose let us study the propagation of a monochromatic relativistic circularly polarized (CP) Alfvén wave. In the limit of small amplitudes the total magnetic field

strength is preserved in time, the Alfvén speed is given by $B_0/\sqrt{w_t}$ and the relation between velocity and magnetic fluctuations reduce to $\delta\mathbf{v} = \pm\delta\mathbf{B}/\sqrt{w_t}$, similarly to the classical MHD case. Define now, at $t = 0$, the various quantities in a generic cartesian reference frame (ξ, η, ζ) as $\rho = 1$, $p = 0.1$, $v_\xi = 0$, $B_\xi = B_0 = 1$, and

$$v_\eta = A \cos(2\pi\xi), \quad v_\zeta = A \sin(2\pi\xi),$$

where $B_\eta = -v_\eta$, $B_\zeta = -v_\zeta$, and $A = 0.01$. In the 1-D case we simply have $(\xi, \eta, \zeta) = (x, y, z)$, whereas in the 2-D case we consider propagation along the $x = y$ direction, so that $(\xi, \eta, \zeta) = ((x + y)/\sqrt{2}, (-x + y)/\sqrt{2}, z)$. In both cases $[0, 1]$ intervals and periodic bound-

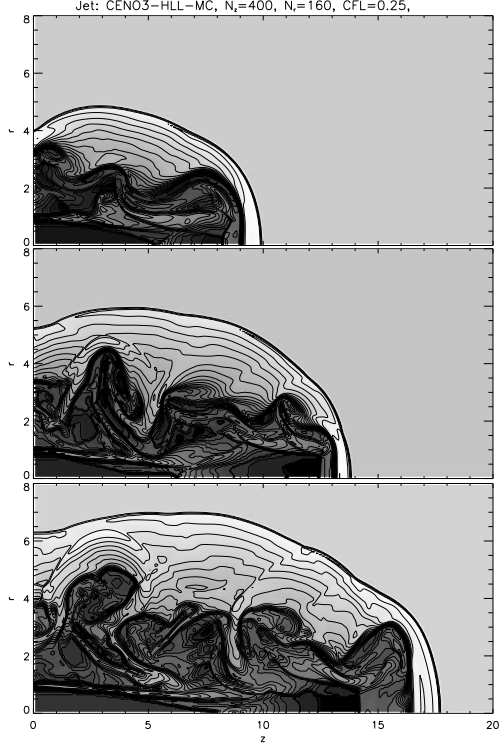


Fig. 3. Density grayscale plots (logarithmic) of the simulation of a relativistic HD jet for times $t = 20, 30, 40$ in 2-D cylindrical geometry.

ary conditions have been assumed, so that after one period $t = T$ the wave should return unchanged to the initial position, as long as transverse relativistic effects can be neglected (they scale as $A^2 = 10^{-4}$). In 1-D $B_0 = 1$ and the wave period is $T = 1$, while in 2-D we take $B_0 = \sqrt{2} \Rightarrow B_{0x} = B_{0y} = 1$, so that two complete spatial periods are set along the main diagonal $x = y$ and therefore $T = 0.5$.

Third order convergence, in time and space, can thus be proved by measuring relative errors of a certain quantity, v_z in our case, at different resolutions, where the error is here evaluated as the L_1 norm of the numerical solution after one period T , compared to the initial settings. In Fig. 4 the errors are plotted in both 1-D and 2-D cases as a function of the number of grid points employed $N = N_x = N_y$, in logarithmic scale. As expected, third order

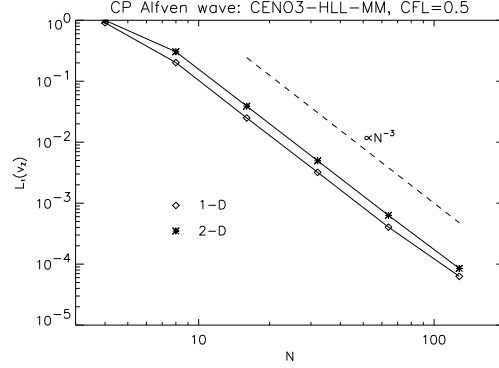


Fig. 4. Convergence test for the 1-D and 2-D CP Alfvén wave problem. Relative L_1 errors on v_z are shown in logarithmic scale.

accuracy is achieved, already in low resolution runs. The base scheme employed is CENO3-HLL-MM, which gives the smoothest profiles, more appropriate to wave-like features.

3.3. Code parallelization

For large 2-D and especially 3-D simulations, the code must be parallelized. This had been already done for the original MHD code, and the addition of the relativistic F90 modules has not affected the overall parallel structure. Parallelization was achieved under MPI directives by splitting the z domain in N_{PE} sub-domains, where N_{PE} is the number of processors employed that can be defined at run-time, like the number of grid-points in all directions. The ghost cells technique was used for boundary conditions, so that communication among consecutive sub-domains is naturally achieved thanks to the use of *send-receive* directives. The only other two places where parallel directives are needed are I/O routines and in the definition of the global time-stepping increment dt .

In Fig. 5 the speed-up factor is shown for two different sets of resolutions. As we can see, when sufficient grid points are present in each z sub-domain, scalability is almost perfect. The data plotted refer to test runs on the Cineca Cray T3E, now dismissed. However, the use of the MPI standard makes our code portable

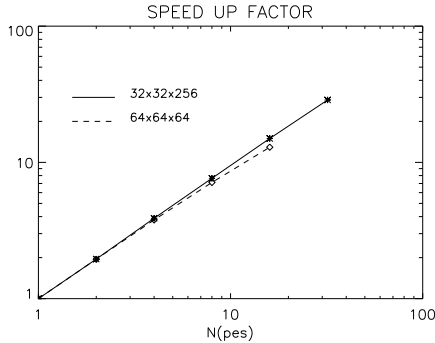


Fig. 5. The speedup factor as a function of the number of processors N , in logarithmic scale. Parallelization (with MPI) has been achieved by splitting the z domain in N sub-domains. When these have a sufficient number of grid points in z , say 10, scalability is almost perfect.

and equivalent performances are obtained on all other Cineca platforms (IBM SP4, Beowulf Linux cluster).

4. Axisymmetric simulations of Pulsar Wind Nebulae

Pulsar Wind Nebulae, or plerions, are bubbles of hot plasma emitting synchrotron and Inverse Compton basically at all frequencies, from radio to X and even γ -rays. They are originated from the confinement by the expanding Supernova Remnant (SNR) of the ultrarelativistic, magnetized wind powered by the pulsar spin-down energy. The best studied plerion is the Crab Nebula, where new spatial features in the inner region have been recently discovered by the X-ray *Chandra* satellite (Weisskopf et al. 2000; Hester et al. 2002), namely an equatorial bright torus and two polar jet-like features with supersonic velocities ($v \approx 0.5 - 0.7c$). Similar features have been later discovered in a growing number of other objects.

While the presence of an X-ray torus may be at least qualitatively explained within the framework of standard 1-D RMHD models (Kennel & Coroniti 1984), if we further assume that the energy flux emerging from the pulsar is higher at low latitudes around the equator, the presence of jets that seem to em-

inate directly from the pulsar poses severe theoretical problems in its interpretation, given the difficulties at explaining self-collimation of ultra-relativistic flows. A recent suggestion for an answer to this puzzle (Bogovalov & Khangoulia 2002; Lyubarsky 2002) is that the jets are actually originating downstream of the pulsar wind termination shock, where the flow is only mildly or non-relativistic and the magnetic field is compressed even beyond equipartition. The wind anisotropy causes to termination shock to assume an oblate shape, the post-shock outflow is thus focussed in the equatorial plane, where magnetic hoop stresses finally divert this flow toward the axis to produce the observed jets (Lyubarsky 2002).

Thanks to the recent progress in numerical RMHD, as described above, we are now able to start a more quantitative investigation of this problem by means of computer simulations (see Amato et al. 2003 for preliminary results and Del Zanna et al. *submitted*). A similar numerical investigation has been recently carried out (Komissarov & Lyubarsky 2003), confirming the basic physical picture as viable for explaining the main observational features, as strongly suggested also by the close resemblance, at least at a qualitative level, between the map of simulated emission and *Chandra* images of the Crab Nebula.

The initial conditions of our axisymmetric simulations are as follows. The ultrarelativistic pulsar wind is set up within an arbitrary radius of 0.2 light years (the domain, in spherical coordinates, is $0.05 < r < 20$ in radius and $0 < \theta < \pi/2$ in the polar angle). The energy flux latitude dependence is introduced as a dependence on θ of the wind Lorentz factor γ , namely:

$$\gamma(\theta) = \gamma_0[\alpha + (1 - \alpha) \sin^2 \theta],$$

where the subscript 0 indicates quantities in the equatorial plane, and $\alpha \leq 1$ is a parameter controlling the ratio between the Lorentz factor at the pole and that at the equator. Here we take $\gamma_0 = 100$ and $\alpha = 0.1$. We then assume the streamlines to be radial upstream of the shock and the mass flux to be isotropic (Bogovalov & Khangoulia 2002). The residual magnetic

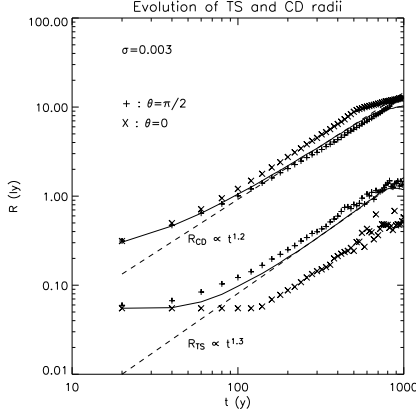


Fig. 6. The time evolution of the PWN boundaries, the TS and CD radii, for $\theta = \pi/2$ and $\theta = 0$ (symbols as indicated on the plot), in the $\sigma = 0.003$ case.

field in the wind is purely toroidal and it is defined as $B(r, \theta) \sim \sin \theta / r$. The total wind energy flux may then be written as

$$F(r, \theta) \sim [\alpha + (1 - \alpha + \sigma) \sin^2 \theta] / r^2,$$

where σ is the parameter defining the wind magnetization, that is the ratio between Poynting and kinetic energy fluxes (at the equator). Around the wind region, a shell of cold ejecta in self-similar expansion is set up, surrounded by a static interstellar medium (ISM).

The spatial grid is made up by 400 cells in r and 100 cells in θ , and a logarithmic stretching ($dr \sim r$) is imposed to better resolve the inner region (notice that this choice leads to extremely small timesteps). Stationary conditions for all quantities are imposed at the inner radius, where the super-fastmagnetosonic wind is blowing from, while zeroth order extrapolation is assumed at the outer boundary.

4.1. Simulation results and discussion

The PWN evolution is followed up to $t = 1000$ years for four cases with different magnetization: $\sigma = 0.003$, $\sigma = 0.01$, $\sigma = 0.03$, and $\sigma = 0.1$. After a short (a few years) transient stage during which, after the nebula is first formed,

the reverse shock propagates backward, both the wind termination shock and the contact discontinuity (the latter separates the nebula from the swept up shell of ejecta) move outward. In Fig. 6 the evolution of the PWN boundaries for $\theta = \pi/2$ and $\theta = 0$ is plotted against time, in the $\sigma = 0.003$ case. For a comparison, also the correspondent 1-D spherically symmetric evolution is shown, together with the fits expected for (hydrodynamical) self-similar models of PWN interacting with freely expanding SN ejecta. At later times ($t \approx 500$ years in this case) the expected self-similar expansion is slowed down because of the interaction with the reverse shock produced by the motion of the SNR in the surrounding ISM. This is the beginning of the so called *reverberation* phase (see Bucciantini et al. 2003), here occurring rather early because of the high spin-down luminosity adopted ($\sim 5 \times 10^{39}$ erg/s).

As expected, the PWN inner boundary (the termination shock, TS hereafter) is farther from the pulsar at the equator than at the pole, while the opposite occurs at the outer boundary (the contact discontinuity, CD hereafter). The former effect is due to the assumed wind energy flux anisotropy which produces the oblate shape of the TS. The latter effect is due, instead, to the pinching by the PWN magnetic field (Begelman & Li 1992).

The detailed structure of the flow in the vicinities of the TS is shown in Fig. 7, where its complexity is apparent. Here we show the different regimes of the post-shock flow: in region D, due to the obliquity of the TS, the speed remains super-fastmagnetosonic, until the plasma crosses the *rim shock* b and it is finally slowed down to sub-fastmagnetosonic speeds in the funnel C.

Let us now investigate how the flow pattern inside the PWN is affected by the nebula magnetization. In Fig. 8 we show the speed magnitude and the streamlines for increasing values of σ , namely 0.003, 0.01 and 0.03, at the same time $t = 400$. The jet is basically absent in the low magnetization case, where only a subsonic flow ($v < 0.1c$) is observed along the polar axis. In the intermediate case the polar outflow starts to be more collimated and its speed increases to supersonic velocities. Finally, in the

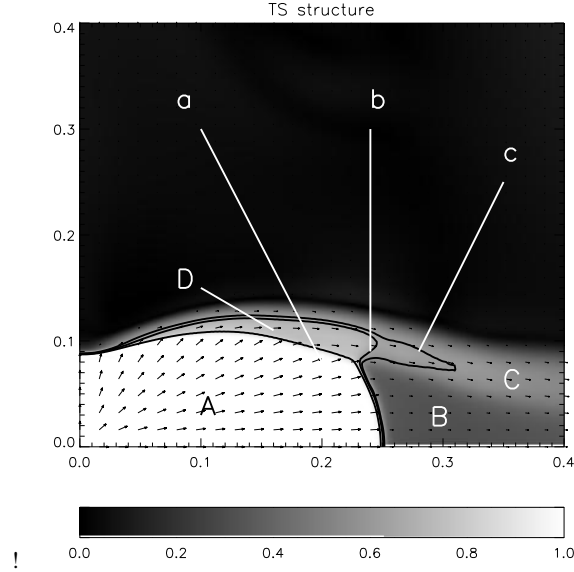


Fig. 7. The flow structure around the TS. The background 2-D gray-scale plot refers to the velocity magnitude. The arrows indicate the streamlines. Labels refer to: A) ultrarelativistic wind region; B) subsonic equatorial outflow; C) equatorial supersonic funnel; D) super-fastmagnetosonic shocked outflow; a) termination shock front; b) *rim shock*; c) fastmagnetosonic surface.

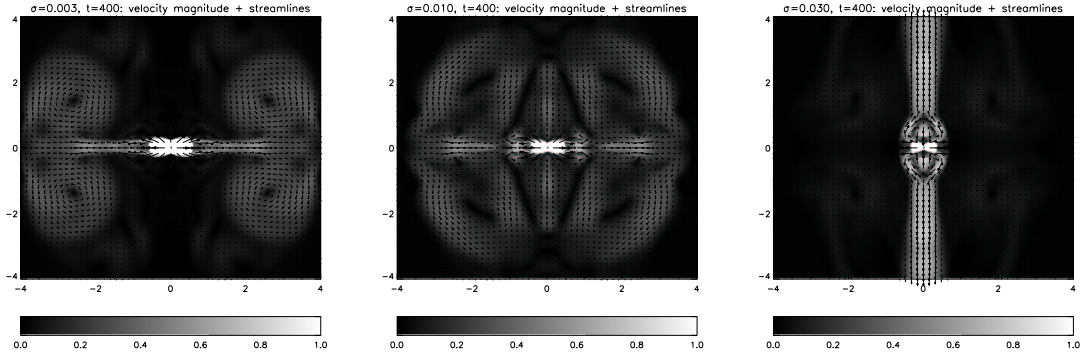


Fig. 8. Flow magnitude (gray scale images) and streamlines at time $t = 400$ for three values of the wind magnetization parameter σ . The jet starts to form for $\sigma = 0.01$ and it is very well developed for higher values.

high magnetization case, a strong, well collimated jet is clearly apparent. It has supersonic speed reaching values as high as $v \approx 0.7 - 0.8c$.

The presence of the polar jet seems to be directly correlated to the flow pattern in the rest of the nebula. In the first two cases an equato-

rial flow with speeds $v \approx 0.5c$ is present, together with large scale vortices at higher latitudes. The fast equatorial flow is entirely due to 2-D (basically hydro) effects, since the streamlines bend toward the equator after crossing the oblate TS (see Fig. 7). The vortices oc-

cur when this equatorial flow hits the expanding CD boundary and a circulating back-flow is created. With increasing value of the wind magnetization the equatorial outflow is progressively suppressed. For $\sigma = 0.03$ the flow in the equatorial plane is limited to the close vicinities of the TS. A situation very similar to the latter is found in the highest magnetization case we considered, $\sigma = 0.1$, which is not displayed in the figure. Thus, the mechanism of jet formation is as follows: for high enough values of the wind magnetization (approximately $\sigma > 0.01$, as also found by Komissarov & Lyubarsky using different settings) the equatorial outflow downstream of the TS can be completely suppressed by hoop stresses and diverted toward the polar axis, where part of it will compress the plasma and then drive a super-fastmagnetosonic polar jet.

5. Conclusions

An efficient and easy to implement central-type scheme for special relativistic MHD has been described and tested. Reconstruction is achieved component-wise and a simple two-speed approximate Riemann solver is employed in flux computation. For smooth flows, the overall scheme is third order accurate in both time and space. The code is parallelized with MPI library calls. Future improvements are an AMR version and the extension to General Relativity. As a first astrophysical application, axisymmetric simulations of Pulsar Wind Nebulae in Supernova Remnants aimed at investigating the jet-torus structure as observed in the Crab Nebula have been shown. The results confirm that an anisotropic, magnetized pulsar wind can produce the observed features downstream of the wind termination shock.

References

- Amato E., Del Zanna L., Bucciantini N., 2003, IAUS, 218 *in press*
- Aloy M.A., Ibañez J.M., Martí J.M., Müller E., 1999, ApJ. Suppl., 122, 151
- Begelman M.C., Li Z.-Y. 1992, ApJ., 397, 187
- Bogovalov S.V., Khangoulia D.V., 2002, MNRAS, 336, 53
- Bucciantini N., Blondin J.M., Del Zanna L., Amato E., 2003, A&A, 405, 617
- Del Zanna L., Bucciantini N., 2002, A&A, 390, 1177
- Del Zanna L., Bucciantini N., Londrillo P., 2003a, A&A, 400, 397 (DZ)
- Del Zanna L., Bucciantini N., Londrillo P., 2003b, Mem. SAI Suppl., 1, 165
- Del Zanna L., Amato E., Bucciantini N., 2004, A&A, *submitted*
- Donat R., Font J.A., Ibañez J.M., Marquina A., 1998, J. Comput. Phys., 146, 58
- Evans C., Hawley J.F., 1988, ApJ., 332, 659
- Font J.A., 2003, Living Reviews in Astrophysics
- Gammie C.F., McKinney J.C., Toth G., 2003, ApJ., 589, 444
- Harten A., Lax P.D., Van Leer B., 1983, SIAM rev., 25, 35
- Hester J.J. et al., 1995, ApJ., 577, L49
- Kennel C.F., Coroniti F.V., 1984, ApJ., 283, 694
- Koide S., Nishikawa K.-I., Mutel R.L., 1996, ApJ., 463, L71
- Koide S., Shibata K., Kudoh T., 1999, ApJ., 522, 727
- Komissarov S.S., 1999, MNRAS, 303, 343
- Komissarov S.S., Lyubarsky Y.E., 2003, MNRAS, 344, L93
- Liu X.-D., Osher S., 1998, J. Comput. Phys., 142, 304
- Londrillo P., Del Zanna L., 2000, ApJ., 530, 508
- Londrillo P., Del Zanna L., 2004, J. Comput. Phys., *in press* (arXiv:astro-ph/0310183)
- Lyubarsky Y.E., 2002, MNRAS, 329, L34
- Martí J.M., Müller E., 2003, Living Reviews in Astrophysics
- Shu C.-W., Osher S., 1988, J. Comput. Phys., 77, 439
- Tóth G., 2000, J. Comput. Phys., 161, 605
- Weisskopf M.C. et al., 2000, ApJ., 536, L81